



Structuring phase junction between tri-*s*-triazine and triazine crystalline C₃N₄ for efficient photocatalytic hydrogen evolution

Zhenxing Zeng, Hongtao Yu, Xie Quan*, Shuo Chen, Shushen Zhang

Key Laboratory of Industrial Ecology and Environmental Engineering (Ministry of Education), School of Environmental Science and Technology, Dalian University of Technology, Dalian 116024, China



ARTICLE INFO

Keywords:

Crystalline carbon nitride
Phase junction
Photocatalytic
Hydrogen evolution

ABSTRACT

Herein a novel carbon nitride composite with triazine-based crystalline carbon nitride (tri-C₃N₄) vertically aligned on tri-*s*-triazine-based crystalline carbon nitride (tri-*s*-tri-C₃N₄) is first proposed for efficient visible light driven ($\lambda > 420$ nm) photocatalytic H₂ evolution. The well matched lattice fringes between (002) plane of tri-*s*-tri-C₃N₄ and (102) plane of tri-C₃N₄ characterized by TEM unambiguously demonstrate the successful construction of tight crystalline junction between tri-*s*-tri-C₃N₄ and tri-C₃N₄. As a result, the crystalline carbon nitride phase junction (tri-/tri-*s*-tri-C₃N₄) shows a high visible light photocatalytic H₂ evolution activity of 144 $\mu\text{mol}/\text{h}$, which is 30 times higher than that of pristine g-C₃N₄. This outstanding photocatalytic H₂ evolution performance could be attributed to the fact that the construction of crystalline tight junction can greatly enhance the transfer and separation efficiency of photoinduced carriers. This study may provide a new way for rational design of carbon nitride heterojunction for gaining high photocatalytic activity.

1. Introduction

Photocatalytic water splitting to produce renewable fuel H₂ has been considered as a promising strategy to address the increasingly serious energy crises [1–3]. Recently, graphitic carbon nitride (g-C₃N₄) as a metal-free semiconductor has emerged as a rising star among various photocatalysts for visible light water splitting owing to its unique properties, such as easy accessible, durable for long time operation, suitable energy structure for overall water splitting and composed with earth abundant elements only [4–6]. However, the photocatalytic performance of pristine g-C₃N₄ is severely limited by the intrinsic drawbacks, such as low charge mobility and fast recombination of charge, which largely depends on the intrinsic electronic and structural character of the materials [6,7].

Various strategies, such as heterojunction construction [7–9], co-polymerization [10–12], doping [13,14], nanostructuring [15–19], surface engineering [20–22] and improving crystalline degree [23,24] have been developed to improve the photocatalytic performance of g-C₃N₄. Among them, interfacing g-C₃N₄ with another semiconductor to create a heterojunction structure is an effective way and generally adopted to enhance the separation efficiency of electron-hole pairs and to further improve the solar light conversion efficiency [9,25]. Such a heterojunction structure with a unique energy landscape not only benefits the dissociation of excitons into hot electrons and holes, but it

also can facilitate the subsequent collection and separation of electrons and holes at the interface of the two materials, thereby greatly suppress the recombination of electron-hole [26,27]. When constructing tight junctions, we should both consider the energy band configurations and the physicochemical properties between the two semiconductors. Materials with different crystal phases are not only physicochemically similar, but also have matched energy position to form junctions [28–30]. Therefore, constructing phase junction between triazine-based g-C₃N₄ (tri-C₃N₄) and tri-*s*-triazine-based g-C₃N₄ (tri-*s*-tri-C₃N₄) should be an effective way to form a tight junction.

In generally, photoinduced electron-hole pairs are dissociated and separated at the interface of the two semiconductors, enlarging the effective junction area is therefore important for gaining high photocatalytic performance. Improving the crystallinity of g-C₃N₄ to form a crystalline g-C₃N₄ phase junction would be a great strategy to achieve that goal [31–35]. Such a crystalline structure features lower charge recombination sites, reduced charge transfer blocking sites and improved charge mobility, thus exhibit an enhanced diffusion distance of photo-induced charge carriers [32,36,37]. With an enhanced diffusion distance, more charge carriers are accessible to the junction area for directional separation and subsequently participate in the redox reactions, thereby showing an enhanced photocatalytic performance. In this way, such a crystalline carbon nitride junction material may possess the full potential for overall water splitting [38,39]. Though the fabrication

* Corresponding author.

E-mail address: quanxie@dlut.edu.cn (X. Quan).

of tri-*s*-triazine-based $g\text{-C}_3\text{N}_4$ homojunctions have been reported, most of them were amorphous phases and the construction of crystalline phase junction between tri-*s*-triazine and triazine-based $g\text{-C}_3\text{N}_4$ has been never reported so far.

Here, we for the first time report a secondary growth method for the successful synthesis of crystalline carbon nitride phase junction (tri-/tri-*s*-tri- C_3N_4) with triazin-based crystalline carbon nitride (tri- C_3N_4) vertically aligned on tri-*s*-triazine-based crystalline carbon nitride (tri-*s*-tri- C_3N_4). This unique morphology integrates the advantages of offering a long optical path for light harvest, increased active sites and reduced mass transfer resistance. With tight contact interfaces, enhanced light harvest and improved crystallinity, tri-/tri-*s*-tri- C_3N_4 demonstrates a dramatically enhanced hydrogen evolution rate (HER) than that of pristine $g\text{-C}_3\text{N}_4$ under visible light irradiation. This study may provide a new approach for rational design of carbon nitride junction for simultaneous improving charge mobility and charge separation efficiency for high photocatalytic performance.

2. Experimental

2.1. Preparation of $g\text{-C}_3\text{N}_4$

Pristine $g\text{-C}_3\text{N}_4$ was fabricated by directly heating melamine in a muffle. Generally, melamine (8 g) was put into an alumina crucible with a cover and then heated to 550 °C with a heating rate of 12 °C/min, holding this temperature for 4 h. After natural cooling to room temperature, the yellow powder was obtained.

2.2. Preparation of tri- C_3N_4

For the fabrication of tri- C_3N_4 , melamine (600 mg) was fine ground with a eutectic mixture (2.7 g of LiCl and 3.3 g of KCl), then the mixture was heated to 550 °C at a heating rate of 12 °C/min under Ar atmosphere and then hold this temperature for another 4 h. The final material was obtained after drying the boiling water washed yellow powder overnight at 60 °C.

2.3. Preparation of tri-/tri-*s*-tri- C_3N_4

Melamine (8 g) was put into an alumina crucible with a cover and then heated to 500 °C with a heating rate of 12 °C/min, holding this temperature for 4 h. Then 600 mg of pretreated melamine and a certain amount of melamine (30, 60, 90, 110 mg) were fine ground with the eutectic mixture (2.7 g of LiCl and 3.3 g of KCl), subsequently, the mixture was heated to 550 °C under Ar atmosphere at a heating rate of 12 °C/min and kept for 4 h. After washing with boiling water for several times and dried at 60 °C overnight, the resulting powder were obtained and donated as tri-/tri-*s*-tri- C_3N_4 -x, where x refers to 30, 60, 90, 110 (adding amount of melamine, mg), respectively.

2.4. Preparation of tri-*s*-tri- C_3N_4

Tri-*s*-tri- C_3N_4 was fabricated following the same synthetic procedure of tri-/tri-*s*-tri- C_3N_4 except for the addition of any melamine.

2.5. Characterizations

Morphologies of the as-prepared photocatalysts were investigated by Scanning electron microscopy (SEM, S4800) and Transmission electron microscopy (TEM, Tecnai G2 F30 S-Twin, at an accelerating voltage of 200 kV). Crystal structures of the samples were revealed using a D8 ADVANCE Powder X-ray diffraction (XRD) diffractometer which equipped with a Co-K α radiation. Fourier transform infrared (FTIR) spectra were recorded on a Bruker VERTEX 70 FTIR apparatus with KBr as a reference sample. The chemical states and elemental contents was investigated using a VGESCALAB250 X-ray photoelectron spectrometer

(XPS) with a monochromated Al-K α source at a residual gas pressure of less than 10–8 Pa. Ultraviolet-visible/diffuse reflectance spectroscopy (UV-vis/DRS) was conducted using a Shimadzu UV-2450 spectrophotometer with BaSO₄ as a reference sample. Photoluminescence (PL) measurements were carried out on a HITACHI F-4500 fluorescence spectrophotometer with an excitation wavelength of 330 nm. The time-resolved fluorescence decay spectra were measure under the excitation wavelength of 445 nm on a Time Resolved Fluorescence Spectrometers (FLSP980). Electrochemical measurements were measured in Na₂SO₄ electrolyte (0.1 M) using the electrochemical station (CHI660D, Shanghai Chenhua Limited, China) with a conventional three-electrode configuration.

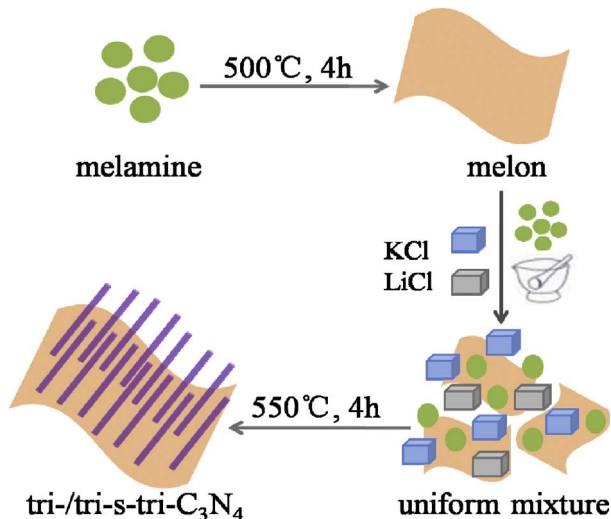
2.6. Photocatalytic experiments

Water splitting reactions were carried out in a Pyrex top-irradiation reaction vessel connected to a glass closed gas system. For each experiment, 50 mg of catalyst was dispersed into 100 mL of an aqueous solution containing 10 mL of sacrificial agent and 3% of Pt was loaded on the surface of materials to boost hydrogen evolution. Prior to the light irradiation, the system was evacuated for several times to completely remove the air. Visible light was served by a 300 W Xenon lamp equipped with a long pass wavelength filter of $\lambda > 420$ nm. The temperature of the reaction system was maintained at 10 °C using a flow of cooling water. The evolved gases were in situ analyzed by a TCD and 5 Å molecular sieve column equipped gas chromatograph (GC-14), argon was used as carrier gas.

3. Results and discussion

3.1. Morphology and formation mechanism

Crystalline tri-*s*-tri- C_3N_4 or tri-/tri-*s*-tri- C_3N_4 -x were synthesized via an ionothermal synthetic route [32]. As shown in Scheme 1, melamine was firstly condensed at 500 °C to gain a treated melamine (melon). Then, the pretreated melamine was mixed with a certain amount of melamine and then ground with an eutectic mixture of KCl/LiCl (KCl: 3.3 g, LiCl: 2.7 g) to form a uniform powder. After treating the mixture at 550 °C for 4 h, crystalline samples can be obtained. The atomic structure of $g\text{-C}_3\text{N}_4$, tri-*s*-tri- C_3N_4 and tri- C_3N_4 are shown in Fig. S1. SEM images (Fig. 1) and TEM patterns (Fig. S2) show that $g\text{-C}_3\text{N}_4$ and tri-*s*-tri- C_3N_4 feature a lamella structure, while tri- C_3N_4 demonstrates a nanorod morphology. These results are in consistent with the previously reported results. The phase junction materials clearly show that



Scheme 1. Illustration of the preparation process of crystalline carbon nitride phase junction tri-/tri-*s*-tri- C_3N_4 .

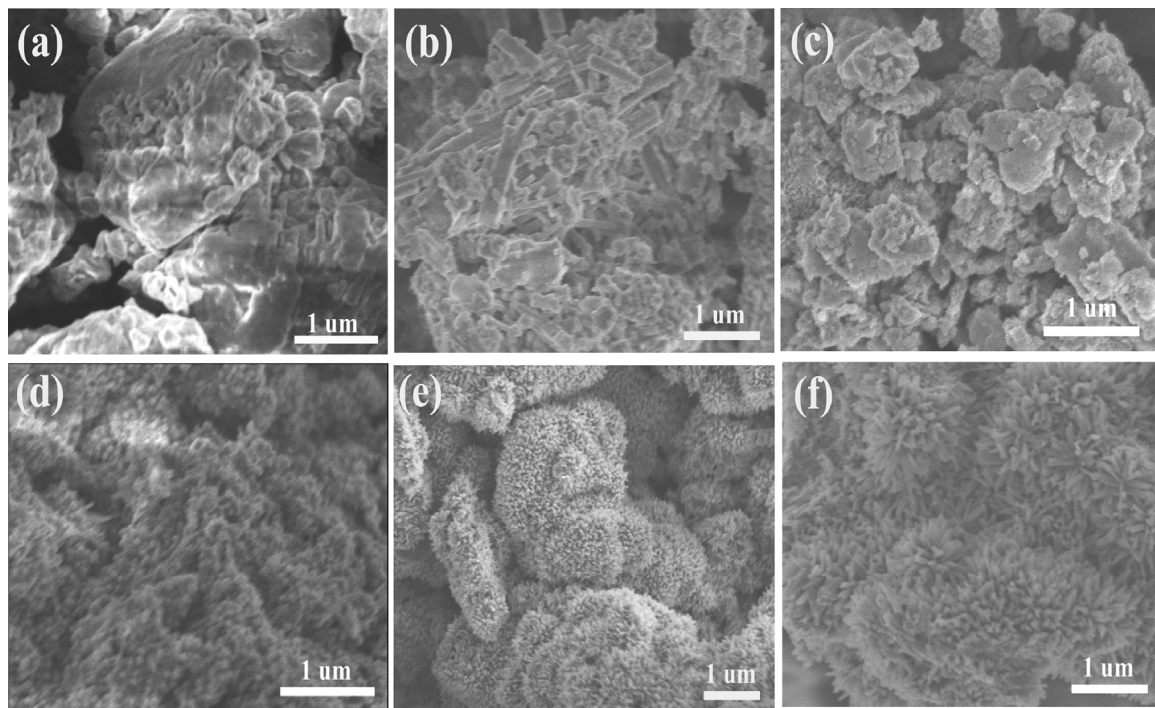


Fig. 1. Typical SEM images of as-prepared samples: (a) $\text{g-C}_3\text{N}_4$, (b) $\text{tri-C}_3\text{N}_4$, (c) $\text{tri-s-tri-C}_3\text{N}_4$, (d) $\text{tri-/tri-s-tri-C}_3\text{N}_4\text{-30}$, (e) $\text{tri-/tri-s-tri-C}_3\text{N}_4\text{-60}$ and (f) $\text{tri-/tri-s-tri-C}_3\text{N}_4\text{-90}$.

$\text{tri-C}_3\text{N}_4$ is a nanorod structure with a size of several tens of nanometers and vertically aligned on $\text{tri-s-tri-C}_3\text{N}_4$. With alerting the secondary adding amount of melamine, the morphology of $\text{tri-C}_3\text{N}_4$ evolved from nanodots to nanoneedles and eventually to nanorods. Note that, melamine start to melt when the temperature raised to 330°C and thus can sufficient contact with the surface amino groups of melon, this should be a fundamental requirement for the intimate contact between $\text{tri-C}_3\text{N}_4$ and $\text{tri-s-tri-C}_3\text{N}_4$ [36]. The melted melamine firstly condensed with the surface amino groups to form an occupied condensation sites, subsequently start to grow within the void of the molten salt and eventually forming a vertically aligned morphology [40]. Thinking that, such a vertically aligned nanorod structure offers a long optical path for light harvesting, provides more catalytic sites and reduces mass transfer resistant, thus benefit for photocatalytic performance [41–43]. To the best of our knowledge, this should be the first successful fabrication of such a vertically aligned crystalline carbon nitride phase junction structure.

3.2. Structure information

The porosity and surface area of the as-prepared materials were tested by nitrogen gas adsorption-desorption isotherms and pore-size distribution curves analysis (Figs. 2 and S3). All samples exhibit a typical type IV isotherm with a H1-type hysteresis loop and the surface area of these materials are summarized in Table S1. All crystalline materials exhibit a dramatically increased surface area than that of $\text{g-C}_3\text{N}_4$, which may attribute to the creation of pores during the molten salts treatment. As for the junction materials, the surface area increases with the adding amount of melamine and eventually reaches $79.7\text{ m}^2/\text{g}$. However, with excess adding amount of melamine, the surface area decreased, which may attribute to the desultory morphology that partially blocked the pores. The pore size distributions of the as-prepared materials are displayed in the insert of Figs. 2 and S3, benefiting from the ionothermal treatment the crystalline samples show abundant mesopores with pore size ranging from 2 to 18 nm.

XRD was used to confirm the crystal structure of as-prepared samples. Two characterized peaks located at 9.4° and 32.8° can be observed for $\text{tri-s-tri-C}_3\text{N}_4$. The in-plane repeating motifs at 9.4° , correspond to

the (100) plane with a repeating distance of 1.09 nm , whereas peak located at 32.8° is attributed to the (002) reflection of graphitic-like aromatic structure with a distance of 0.318 nm . The typical reflection peak of $\text{tri-C}_3\text{N}_4$ at 34.1° corresponds to the indexed (002) plane with a distance of 0.285 nm [25]. With the construction of crystalline structure, the in-plane periodic repeating motif is more regular, leading to an enhanced extensibility of in-plane structure as confirmed by the lower XRD angle shift of (100) plane. In return, compared to the amorphous structure, a more regular in-plane structure may benefit in layers stacking, thus a denser layer structure is therefore reasonable, the right shift XRD angle of (002) plane further support this claim [44,45]. Moreover, the coexistence of both characterized reflection peaks of $\text{tri-C}_3\text{N}_4$ and $\text{tri-s-tri-C}_3\text{N}_4$ for $\text{tri-/tri-s-tri-C}_3\text{N}_4\text{-90}$, marked in red solid rectangle and green solid cycle (Fig. 3a), powerfully prove the successful construction of both phases. After molten salt treatment, the typical skeleton of carbon nitride remained as characterized by FT-IR in Fig. 3b. Interestingly, an obvious vibration peak can be found at 2170 cm^{-1} for the molten salt treated materials, demonstrating an introduced cyanamide groups in the terminal framework. Besides, the reduced FT-IR vibration intensity around 3200 cm^{-1} of $\text{tri-/tri-s-tri-C}_3\text{N}_4$ means the decrease of existed $-\text{NH}_x$ (which often serves as charge recombination sites).

To further confirm the crystalline structure and the successful construction of junctions, HRTEM measurement was carried out to probe the crystal lattice information. In Fig. 4a, $\text{g-C}_3\text{N}_4$ displays an amorphous structure without any lattice fringe and FFT diffraction spots. Instead of amorphous structure, clearly lattice fringe of $\text{tri-/tri-s-tri-C}_3\text{N}_4\text{-90}$ in Fig. 4b can be observed, which strongly support the crystalline structure of it. Meanwhile, the FFT pattern inserted in Fig. 4b of $\text{tri-/tri-s-tri-C}_3\text{N}_4\text{-90}$ shows sharp diffraction spots, revealing the crystalline nature of the diffraction region. In Fig. 4c and the corresponding lattice fringes, the denoted lattice fringe for 1 with a lattice spacing of 0.315 nm correspond to the interlayer distance of $\text{tri-s-tri-C}_3\text{N}_4$ and marked as (002) plane, while the indexed lattice fringe of 2 with a lattice fringe of 0.290 nm is attributed to the (002) plane of $\text{tri-C}_3\text{N}_4$. The typical lattice spacing is well in agreement with the XRD revealed plane diffraction distances, which again demonstrates the successful preparation of different crystal phase structures. In addition, it can be

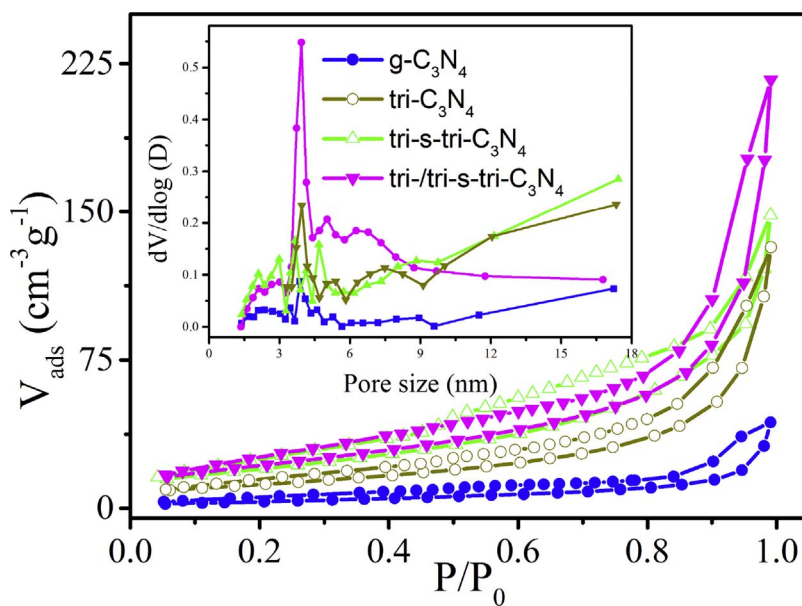


Fig. 2. Nitrogen gas adsorption-desorption isotherms and pore-size distribution curves (inset) of as-prepared materials.

observed in Fig. 4c that the phase junction between tri-s-tri-C₃N₄ and tri-C₃N₄ is composed of well matched lattice fringes between (002) plane of tri-s-tri-C₃N₄ and (002) plane of tri-C₃N₄, thus unambiguously demonstrate the successful construction of tight crystalline junction between tri-s-tri-C₃N₄ and tri-C₃N₄ [46,47].

3.3. Optical and electronic properties

It is necessary to investigate the optical and chemical properties since the crystalline carbon nitride phase junction has been successfully constructed. As shown in Fig. 8, all the crystallized materials show enhanced light absorbance compare to the pristine g-C₃N₄. The tighter and better packing of the joint tri-s-triazine system is helpful to reinforce the $\pi \rightarrow \pi^*$ electron transition, thus resulting in the enhanced light harvest. As we know, improved crystallinity is usually more beneficial in charge transfer, thus showing a reduced charge migration resistance. Electrochemical impedance spectroscopy (EIS) results in Fig. 5a show that each crystalline material exhibits a smaller arc radius, suggesting the reduced electron transfer resistance and higher electron conductivity. Photoluminescence (PL) is another powerful tool to uncover the energy-wasteful charge recombination information. As shown in Fig. 5b, the dramatically weakened emission wavelength intensity suggests a lower recombination rates for each crystalline materials, because most of the charge trapping sites ($-\text{NH}_x$) have been condensed through the molten salt treatment, which is in accordant with the FT-IR results. Another reason is that, the built-in electrical field induced by the junction would facilitate the dissociation of excitons and spacially

locate the electrons and holes on the two semiconductors, therefore suppressing the charge recombination. The improved crystallinity together with the phase junction construction of tri-/tri-s-tri-C₃N₄-90 resulted in rapid charge transfer and separation efficiency. This result is further evidenced by time-resolved transient PL measurements in Fig. 5c. The average PL lifetime of tri-/tri-s-tri-C₃N₄-90 is 1.3 ns, which is 2.6 ns shorter than that of g-C₃N₄ counterpart (3.9 ns). The reduced lifetime of charge indicates the enhanced charge transfer and separation efficiency of the phase junction material, which may therefore increase the possibility of charge to react with the electron or hole captures, leading to an increased photocatalytic performance [48–52]. Combining ESI results with PL analysis, the enhanced charge mobility and reduced electron-hole recombination rates in return can facilitate the photo-induced carriers diffusing to a much longer distance, so that more carriers can reach the junction for directional separation or move to the surface of the material for catalytic reactions before recombination. As the built-in electric field via junction construction can powerfully drive the charge carriers migrate through the interface directionally, an enhanced photocurrent can be observed for tri-/tri-s-tri-C₃N₄-90 in Fig. 5d. Upon light irradiation, all the samples display typical n-type photocurrents, and the photocurrent of tri-/tri-s-tri-C₃N₄-90 is more than two times higher than that of tri-s-tri-C₃N₄, attributed to the improved charge separation efficiency by band offset. Based on the above analysis, the intrinsic drawbacks of low charge mobility and fast electron-hole recombination together with the ineffective charge separation in amorphous g-C₃N₄ have been fully addressed by crystal phase junction construction, so a better photocatalytic performance can

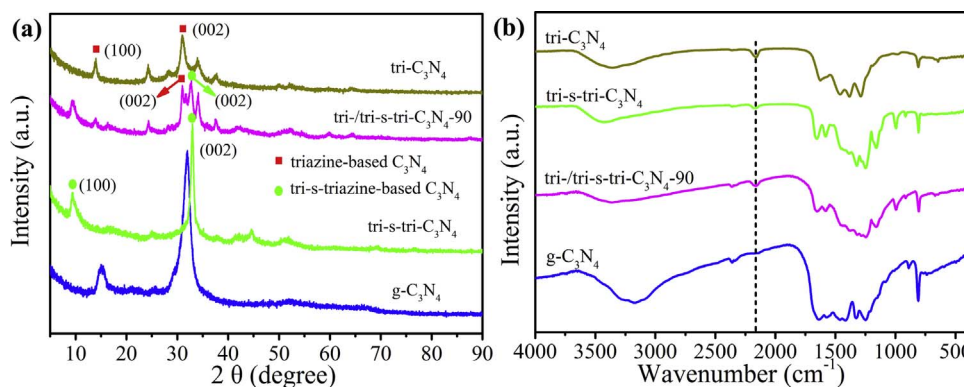


Fig. 3. (a) XRD patterns and (b) FT-IR spectra of g-C₃N₄, tri-C₃N₄, tri-s-tri-C₃N₄ and tri-/tri-s-tri-C₃N₄-90. (the X-ray was served by a Co-K α radiation source).

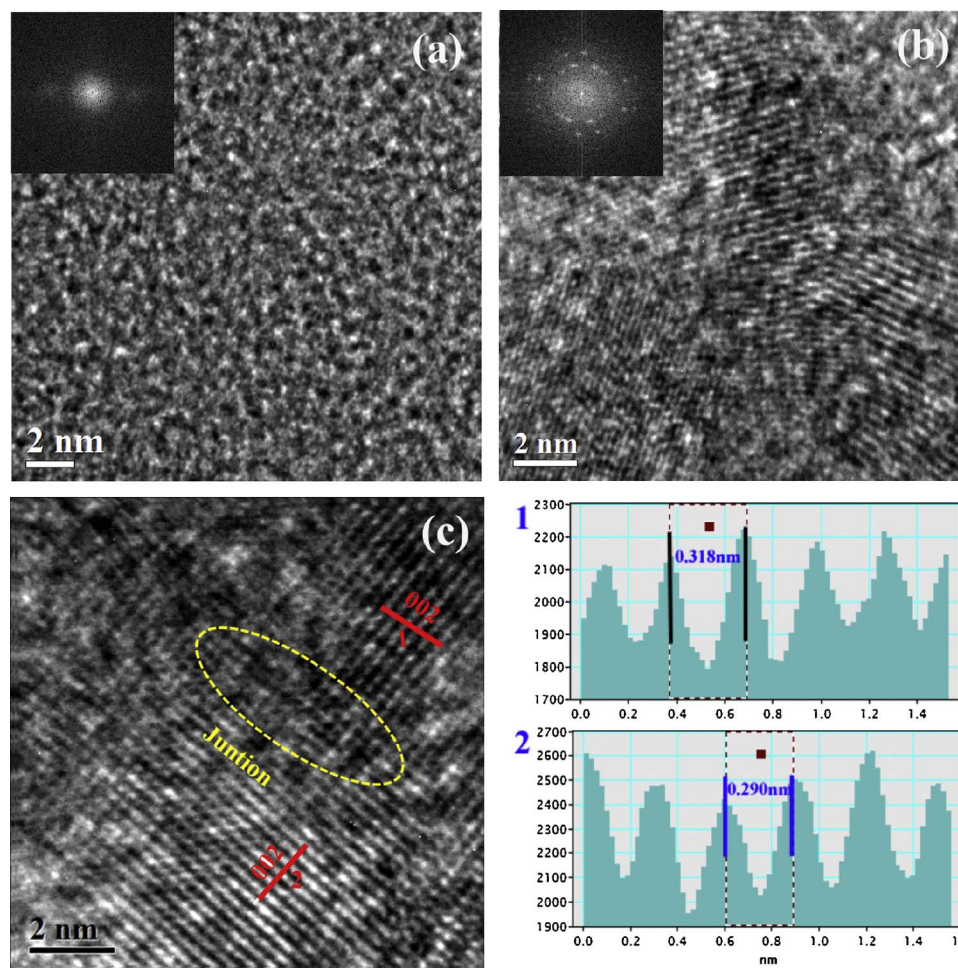


Fig. 4. Typical TEM images of $\text{g-C}_3\text{N}_4$ and tri-/tri-s-tri-C₃N₄-90. (a) HRTEM image of $\text{g-C}_3\text{N}_4$ and corresponding FFT (insert). (b)–(c) HRTEM images of tri-/tri-s-tri-C₃N₄-90 and corresponding FFT (insert). The lattice fringes marked in (c) were shown on the right of it.

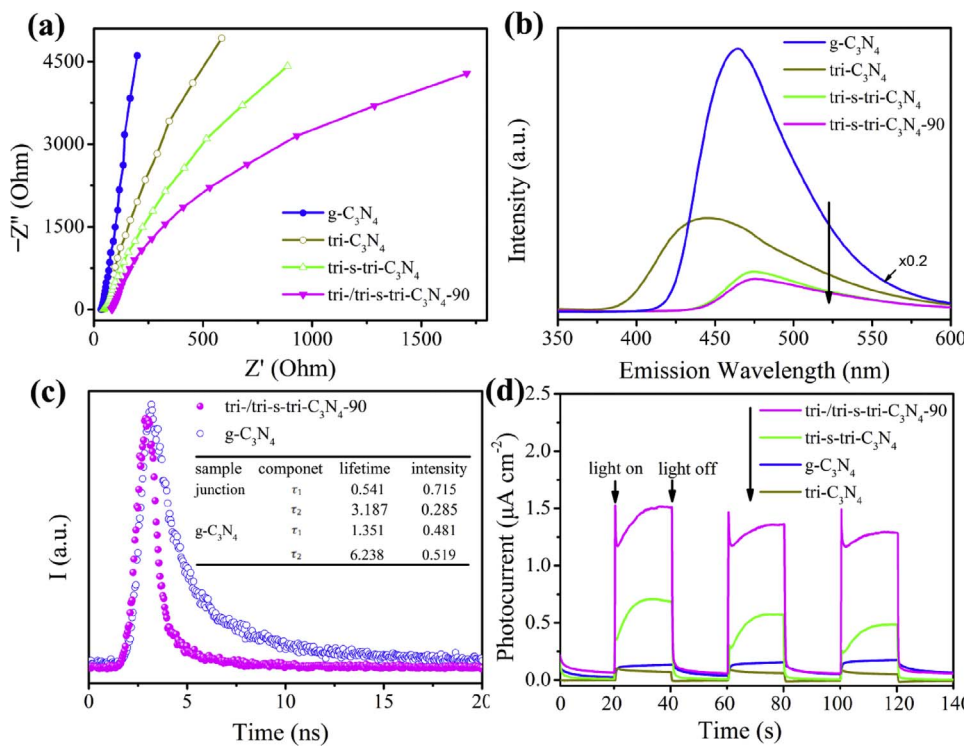
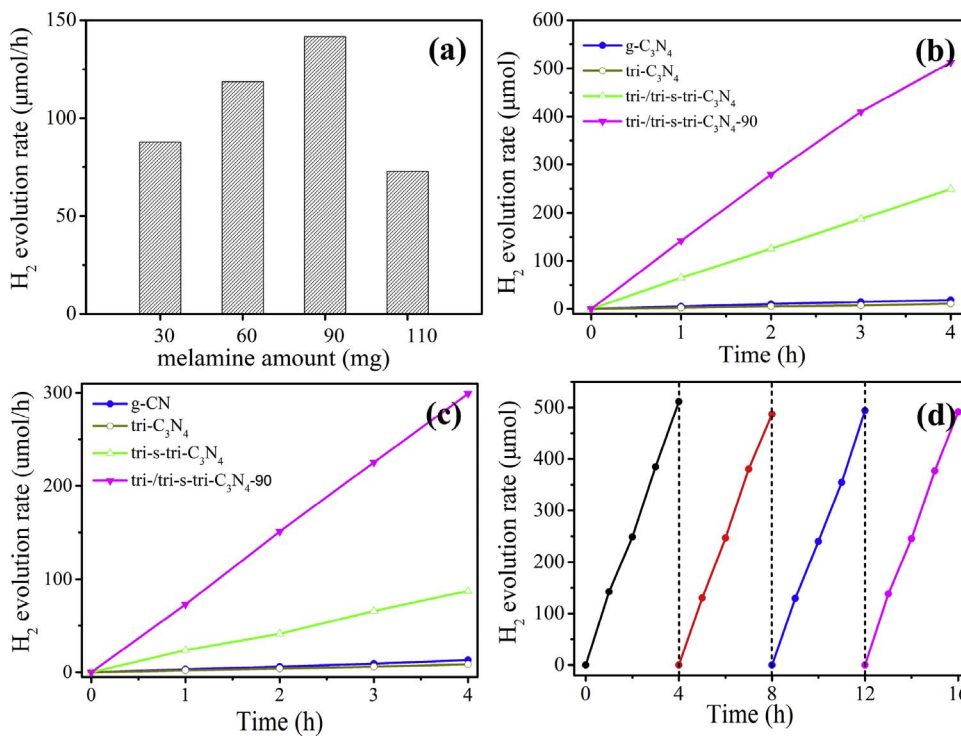


Fig. 5. (a) Nyquist plots of electrochemical impedance spectroscopy, (b) PL spectra, (c) Transient absorption signal decay and (d) Transient photocurrent response of $\text{g-C}_3\text{N}_4$, tri-C₃N₄, tri-s-tri-C₃N₄ and tri-/tri-s-tri-C₃N₄-90.



be naturally expected.

3.4. Photocatalytic hydrogen evolution

Visible light photocatalytic water splitting to produce renewable H₂ was used to evaluate the catalytic performance of as-prepared materials. Before the catalytic reactions, 3 wt% Pt was loaded on to the surface of material to promote H₂ production. We first tested the crystalline carbon nitride phase junctions with different secondary melamine adding amount (tri-/tri-s-tri-C₃N₄-x) by using TEOA (10 vol %) as hole scavenger. In Fig. 6a, as we can see the junction materials display efficient HER performances, and the optimum secondary melamine adding amount is around 90 mg. However, with excess adding amount of melamine, parts of the tri-C₃N₄ are randomly dispersed on the surface of aligned tri-C₃N₄ because the condensation sites are fully occupied by the vertically aligned tri-C₃N₄. This kind of desultory morphology (Fig. S2a) is thought to possess a higher mass transfer resistant and will affect the light incident, thus showing a reduced catalytic activity. Since tri-/tri-s-tri-C₃N₄-90 shows the highest photocatalytic performance, we then chose it as a representative junction material to further investigate the photocatalytic performance. Photocatalytic HER of tri-s-tri-C₃N₄ is much higher than that of pristine g-C₃N₄ (Fig. 6b), which should attribute to the enhanced charge mobility and reduced recombination sites by improving the crystallinity, thus more photo generated carriers can migrate to the surface to participate redox reactions. After further improving the charge separation efficiency by junction formation, the tri-/tri-s-tri-C₃N₄-90 demonstrates excellent HER performance at a rate of 144 μmol/h, which is about 2-fold and near 30-fold higher than tri-s-tri-C₃N₄ and g-C₃N₄, respectively. The apparent quantum Yeild (AQY) of tri-/tri-s-tri-C₃N₄-90 was also investigated and the wavelength dependent AQY for H₂ evolution is shown in Fig. 7. The AQY value at 420 nm reaches 12.9% (TEOA was used as eletron donor), which is much higher than the pristine g-C₃N₄. In addition, the AQY value decreases with the increasing of wavelength, demonstrating the strongly dependent of incident light. The similar catalytic activity trend also can be found when using MeOH as sacrificial agent (Fig. 6c). However, the tri-C₃N₄ still shows a relatively low H₂ evolution performance, which may result from the limited extending

Fig. 6. (a) H₂ evolution rate of crystalline heterojunctions with different melamine adding amount. (b) H₂ evolution rate of g-C₃N₄, tri-C₃N₄, tri-/tri-s-tri-C₃N₄ and tri-/tri-s-tri-C₃N₄-90 using (b) TEOA and (c) MeOH as holes scavenger. (d) Stability test of H₂ evolution for tri-/tri-s-tri-C₃N₄-90 under visible light irradiation by using TEOA as sacrificial agent. Photocatalytic tests were carried out under visible light ($\lambda > 420$ nm) irradiation.

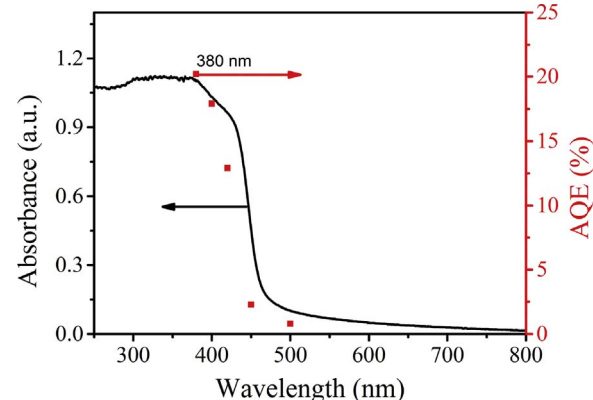


Fig. 7. Wavelength dependent AQY of H₂ evolution over tri-/tri-s-tri-C₃N₄-90 (right axis), UV/vis light absorption spectra of tri-/tri-s-tri-C₃N₄-90 (left axis).

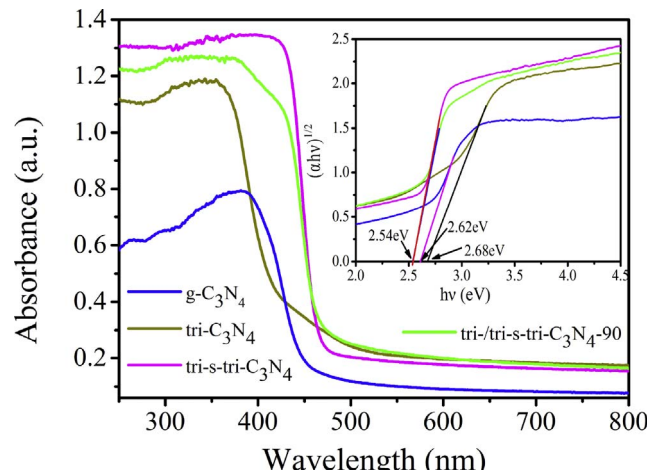


Fig. 8. UV-vis diffuse reflectance spectrum and corresponding Tauc plots (inset) of g-C₃N₄, tri-C₃N₄, tri-s-tri-C₃N₄ and tri-/tri-s-tri-C₃N₄-90.

of aromatic rings and low visible light harvest.

To verify the claim that the dramatic enhancement of HER performance of junction material is originated from the crystalline junction construction rather than other reasons, several control experiments were carried out (Fig. S4). Firstly, no significant photocatalytic improvement can be found for the physical mixed sample tri-C₃N₄ + tri-s-tri-C₃N₄-90, strongly prove the importance of junction formation. Secondly, we fabricated an amorphous carbon nitride homojunction g-C₃N₄/g-C₃N₄ according to the previously reported method [53]. Though an enhancement can be observed for this material but it's still 2.8-fold lower than the crystalline junction counterpart. This means that reducing the recombination sites of $-\text{NH}_x$ by improving the crystallinity can enhance the diffusion distance of charge carriers, thus more charge can migrate to the junction area for further separation and leading to an increased photocatalytic performance, which demonstrating the importance of crystalline structure construction. Note that, post annealing treatment can by some sort increase the photocatalytic activity, but it's far away than the promotion by crystalline junction construction. Thirdly, to highlight the importance of tight junction, by using tri-s-tri-C₃N₄ and C, N doped TiO₂, we fabricated the tri-s-tri-C₃N₄/TiO₂-C_xN heterojunction material according to the previously reported method (C and N codoped TiO₂ has visible light response). The reason we chose it as a reference sample is that the C and N codoped TiO₂ shows a similar band gap and similar energy band configuration to that of crystalline carbon nitride [54]. Even with both crystalline components, the photocatalytic performance of this heterojunction material is still low respect to the tri-s-tri-C₃N₄, which may be affected by the different physicochemical properties of carbon nitride and TiO₂, thus showing the importance of physicochemical features between the components. The control experiment results described above thus highlight the significance of constructing crystalline carbon nitride phase junction for high performance photocatalytic hydrogen production. Furthermore, the stability of the junction was tested by four consecutive operations for photocatalytic hydrogen evolution. As seen in Fig. 6d, no obvious deactivation was observed after 16 h photocatalytic reaction, demonstrating a robust stability toward long time photo-corrosion in solution, which may owing to the good compatibility of this two crystal phases. The HRTEM and XRD characterizaion of the sample after cycle experiments in Fig. S5 also confirm the high stability of this junction material.

3.5. Mechanism interpretation

To identify the charge migration between the two phases of tri-C₃N₄/tri-s-tri-C₃N₄-90, Tauc plots and XPS valence band analysis were employed to study the accurate band structure in detail (Figs. 8 and 9). The band gaps of g-C₃N₄, tri-C₃N₄, tri-s-tri-C₃N₄ and tri-s-tri-C₃N₄-90

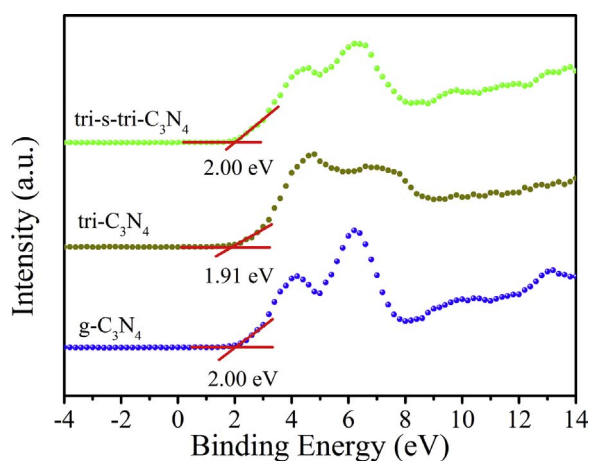


Fig. 9. XPS valence band of g-C₃N₄, tri-C₃N₄, tri-s-tri-C₃N₄ and tri-s-tri-C₃N₄-90.

are tested to be 2.62 eV, 2.68 eV, 2.54 eV and 2.54 eV, respectively. XPS valence band test results in Fig. 9 show that the valence band maximum are located at 1.91 eV for tri-C₃N₄ and about 2.0 eV for the other three materials. Motto-Schottky measurement was employed to determine the flat band of these materials. As shown in Fig. S6, the flat band of g-C₃N₄, tri-C₃N₄ and tri-s-tri-C₃N₄ were measured to be -0.89 eV, -1.53 eV and -1.43 eV respectively. Combining the XPS valence band results and Motto-Schottky plots, the VB position of these materials were calculated to be 1.11 eV, 1.21 eV and 0.95 eV (vs. SCE), respectively. Based on the above analysis, a possible electron and hole migration mechanism of tri-s-tri-C₃N₄-90 is proposed, as illustrated in Fig. S7 [55,56]. Upon visible light irradiation ($\lambda > 420$ nm), both crystalline phases can be excited with electron transited to conduction band (CB), leaving a corresponding hole on valence band (VB), then electron on CB of tri-C₃N₄ transfer to the low CB energy of tri-s-tri-C₃N₄ while hole on the higher VB energy of tri-s-tri-C₃N₄ move to lower VB energy of tri-C₃N₄, forming a type II heterojunctions configuration. Interestingly, we noticed that the light absorbance within excitation edge of each crystalline materials show an unprecedented enhancement in light absorbance, revealed by the DRS result (Fig. 8). XPS was carried out to further investigate the structural information of tri-s-tri-C₃N₄-90, as demonstrated in Fig. S8. The survey spectra reveal the presence of C, N, O, Li, K and Cl elements in tri-s-tri-C₃N₄-90. The C1s spectrum can be fitted into three deconvoluted peaks located at 284.7 eV, 286.8 eV and 288.1 eV, respectively corresponding to the graphitic carbon (C=C=C), primary or secondary amines (C-NH_x) and sp² hybridized C atoms (C=N=C). While for N1s, peak at 398.5 eV corresponds to sp² hybridized aromatic N bonded to carbon atoms (C=N-C), whereas the peak at 399.7 eV is assigned to the tertiary N bonded to carbon atoms in the form of N-(C)₃ and 400.7 eV for $-\text{NH}_x$. The peak with binding energy at 404 eV is attributed to the π excitations [57]. Moreover, the C/N ratio delivered from XPS analysis in Table S2 is about 0.73, which is close to the theoretical value of 0.75, again proving the improved condensation degree. In addition, the introduced Li and Cl elements can be attributed to the coordination within the tri-C₃N₄ structure, which is usual in PTI/Li⁺Cl⁻ [58,59]. Interestingly, K 2p peaks are located at 293.0 eV and 295.7 eV, which is in agreement with the reported binding energy of KN₃ [32,60]. Thus, K⁺ ion is more likely to coordinate with the electron-rich N atoms through ion-dipole interaction within the cavity of carbon nitride. A typical example is the famous C–O cyclic polyether, 18-crown-6, in which the negative charged O exhibits a strong alkali metal ion capture ability to form stable ion-dipole coordination [60]. It has been reported that K⁺ ion is trend to form a z-axis angle with the two dimensional planar (intercalated within the layer), as shown in Fig. S9 [61,62]. In such configuration, the linked K⁺ ions in such unit may delocalize the π electrons of N through Z-axis, and will subsequently facilitate the generation of more charge carrier, thus displaying an enhanced light absorption within excitation light absorption edge. With the enhanced charge mobility and separation efficiency, the increased generation of carriers can be effectively transferred to the surface of the materials, thus increasing the possibility of these carriers to participate the redox reactions, which constitute another possible reason for the high active in hydrogen evolution.

4. Conclusion

In summary, we have successfully fabricated a crystalline carbon nitride phase junction with tri-C₃N₄ nanorods vertically aligned on tri-s-tri-C₃N₄ via a secondary growth method. Improved crystallinity of g-C₃N₄ can largely reduce the charge recombination sites and enhance the charge mobility, therefore more charge carrier can diffuse a longer distance to the junction area for directional separation. Thanks to the similarity in physicochemical properties, a tight junction between tri-C₃N₄ and tri-s-tri-C₃N₄ can be formed, which is beneficial for charge carrier separation. Therefore, tri-s-tri-C₃N₄ demonstrates a

dramatically enhanced visible-light-driven photocatalytic H₂ evolution performance with a rate of 144 μmol/h, which is 30 times higher than that of pristine g-C₃N₄. In addition, the inserted K⁺ ions may delocalize the π electrons thus showing a dramatically enhanced light absorption within excitation light absorption edge. This study may provide a new way for simultaneously improving the charge mobility and separation efficiency of carbon nitride by constructing crystalline phase junction in order to gain high photocatalytic performance.

Acknowledgements

This work was supported by National Natural Science Foundation of China (21590813). Program of Introducing Talents of Discipline to Universities (B13012).

Appendix A. Supplementary data

Supplementary data associated with this article can be found, in the online version, at <https://doi.org/10.1016/j.apcatb.2018.01.023>.

References

- [1] J.A. Turner, *Science* 305 (2004) 972–974.
- [2] J. Low, J. Yu, M. Jaroniec, S. Wageh, A.A. Al-Ghamdi, *Adv. Mater.* (2017).
- [3] D. Voiry, J. Yang, M. Chhowalla, *Adv. Mater.* 28 (2016) 6197–6206.
- [4] X. Wang, K. Maeda, A. Thomas, K. Takanabe, G. Xin, J.M. Carlsson, K. Domen, M. Antonietti, *Nat. Mater.* 8 (2009) 76–80.
- [5] Y. Wang, X. Wang, M. Antonietti, *Angew. Chem. Int. Ed.* 51 (2012) 68–89.
- [6] Y. Zheng, L. Lin, B. Wang, X. Wang, *Angew. Chem. Int. Ed.* 54 (2015) 12868–12884.
- [7] J. Zhang, M. Zhang, R.Q. Sun, X. Wang, *Angew. Chem. Int. Ed.* 124 (2012) 10292–10296.
- [8] S. Cao, J. Low, J. Yu, M. Jaroniec, *Adv. Mater.* 27 (2015) 2150–2176.
- [9] Q. Liang, Z. Li, Y. Bai, Z.H. Huang, F. Kang, Q.H. Yang, *Small* 13 (2017).
- [10] M.K. Bhunia, K. Yamauchi, K. Takanabe, *Angew. Chem. Int. Ed.* 53 (2014) 11001–11005.
- [11] J. Zhang, X. Chen, K. Takanabe, K. Maeda, K. Domen, J.D. Epping, X. Fu, M. Antonietti, X. Wang, *Angew. Chem. Int. Ed.* 49 (2010) 441–444.
- [12] J. Zhang, G. Zhang, X. Chen, S. Lin, L. Möhlmann, G. Dolega, G. Lipner, M. Antonietti, S. Blechert, X. Wang, *Angew. Chem. Int. Ed.* 124 (2012) 3237–3241.
- [13] Y. Wang, J. Zhang, X. Wang, M. Antonietti, H. Li, *Angew. Chem. Int. Ed.* 49 (2010) 3356–3359.
- [14] G. Liu, P. Niu, C. Sun, S.C. Smith, Z. Chen, G.Q. Lu, H.-M. Cheng, *J. Am. Chem. Soc.* 132 (2010) 11642–11648.
- [15] J. Sun, J. Zhang, M. Zhang, M. Antonietti, X. Fu, X. Wang, *Nat. Commun.* (2012) 1139.
- [16] Y.S. Jun, J. Park, S.U. Lee, A. Thomas, W.H. Hong, G.D. Stucky, *Angew. Chem. Int. Ed.* 52 (2013) 11083–11087.
- [17] Q. Liang, Z. Li, X. Yu, Z.H. Huang, F. Kang, Q.H. Yang, *Adv. Mater.* 27 (2015) 4634–4639.
- [18] Q. Han, B. Wang, J. Gao, Z. Cheng, Y. Zhao, Z. Zhang, L. Qu, *ACS Nano* 10 (2016) 2745–2751.
- [19] Z. Tong, D. Yang, Z. Li, Y. Nan, F. Ding, Y. Shen, Z. Jiang, *ACS Nano* 11 (2017) 1103–1112.
- [20] X. She, J. Wu, H. Xu, J. Zhong, Y. Wang, Y. Song, K. Nie, Y. Liu, Y. Yang, M.F. Rodrigues, R. Vajtai, J. Lou, D. Du, H. Li, P.M. Ajayan, *Adv. Energy Mater.* 7 (2017) 1700025.
- [21] X. She, J. Wu, J. Zhong, H. Xu, Y. Yang, R. Vajtai, J. Lou, Y. Liu, D. Du, H. Li, P.M. Ajayan, *Nano Energy* 27 (2016) 138–146.
- [22] H. Xu, J. Yia, X. She, Q. Liu, L. Song, S. Chen, Y. Yang, Y. Song, R. Vajtai, J. Lou, H. Li, S. Yuan, J. Wu, P.M. Ajayan, *Appl. Catal. B: Environ.* 220 (2018) 379–385.
- [23] L. Lin, C. Wang, W. Ren, H. Ou, Y. Zhang, X. Wang, *Chem. Sci.* 8 (2017) 5506–5511.
- [24] H. Ou, P. Yang, L. Lin, M. Anpo, X. Wang, *Angew. Chem. Int. Ed.* 56 (2017) 10905–10910.
- [25] H. Liu, D. Chen, Z. Wang, H. Jing, R. Zhang, *Appl. Catal. B: Environ.* 203 (2017) 300–313.
- [26] J. Zhang, M. Zhang, R.Q. Sun, X. Wang, *Angew. Chem. Int. Ed.* 51 (2012) 10145–10149.
- [27] H. Wang, X. Sun, D. Li, X. Zhang, S. Chen, W. Shao, Y. Tian, Y. Xie, *J. Am. Chem. Soc.* 139 (2017) 2468–2473.
- [28] Y. Ham, K. Maeda, D. Cha, K. Takanabe, K. Domen, *Chem. Asian J.* 8 (2013) 218–224.
- [29] M.J. Bojdys, J.O. Muller, M. Antonietti, A. Thomas, *Chem. Eur. J.* 14 (2008) 8177–8182.
- [30] Y. Zheng, L. Lin, B. Wang, X. Wang, *Angew. Chem. Int. Ed.* 54 (2015) 12868–12884.
- [31] Y. Guo, J. Li, Y. Yuan, L. Li, M. Zhang, C. Zhou, Z. Lin, *Angew. Chem. Int. Ed.* 55 (2016) 14693–14697.
- [32] L. Lin, H. Ou, Y. Zhang, X. Wang, *ACS Catal.* 6 (2016) 3921–3931.
- [33] H. Ou, L. Lin, Y. Zheng, P. Yang, Y. Fang, X. Wang, *Adv. Mater.* 29 (2017).
- [34] G. Zhang, G. Li, Z. Lan, L. Lin, A. Savateev, T. Heil, S. Zafeiratos, X. Wang, M. Antonietti, *Angew. Chem. Int. Ed.* 56 (2017) 13445–13449.
- [35] K. Schwinghammer, M.B. Mesch, V. Duppel, C. Ziegler, J. Senker, B.V. Lotsch, *J. Am. Chem. Soc.* 136 (2014) 1730–1733.
- [36] H. Gao, S. Yan, J. Wang, Y.A. Huang, P. Wang, Z. Li, Z. Zou, *Phys. Chem. Chem. Phys.* 15 (2013) 18077–18084.
- [37] Z. Chen, A. Savateev, S. Pronkin, V. Papaefthimiou, C. Wolff, M.G. Willinger, E. Willinger, D. Neher, M. Antonietti, D. Dontsova, *Adv. Mater.* 29 (2017) 1700555.
- [38] G. Zhang, Z. Lan, X. Wang, *Chem. Sci.* 8 (2017) 5261–5274.
- [39] Z. Pan, Y. Zheng, F. Guo, P. Niu, X. Wang, *ChemSusChem* 10 (2017) 87–90.
- [40] B. Yuan, Z. Chu, G. Li, Z. Jiang, T. Hu, Q. Wang, C. Wang, *J. Mater. Chem. C* 2 (2014) 8212–8215.
- [41] P.M. Rao, L. Cai, C. Liu, I.S. Cho, C.H. Lee, J.M. Weisse, P. Yang, X. Zheng, *Nano Lett.* 14 (2014) 1099–1105.
- [42] N.P. Dasgupta, C. Liu, S. Andrews, F.B. Prinz, P. Yang, *J. Am. Chem. Soc.* 135 (2013) 12932–12935.
- [43] L. Dou, F. Cui, Y. Yu, G. Khanarian, S.W. Eaton, Q. Yang, J. Resasco, C. Schildknecht, K. Schierle-Arndt, P. Yang, *ACS Nano* 10 (2016) 2600–2606.
- [44] M. Zhou, P. Yang, R. Yuan, A.M. Asiri, M. Wakeel, X. Wang, *ChemSusChem* 10 (2017) 4451–4456.
- [45] V.W. Lau, I. Moudrakovski, T. Botari, S. Weinberger, M.B. Mesch, V. Duppel, J. Senker, V. Blum, B.V. Lotsch, *Nat. Commun.* 7 (2016) 12165.
- [46] X. Wang, Q. Xu, M. Li, S. Shen, X. Wang, Y. Wang, Z. Feng, J. Shi, H. Han, C. Li, *Angew. Chem. Int. Ed.* 51 (2012) 13089–13092.
- [47] J. Zhang, Q. Xu, Z. Feng, M. Li, C. Li, *Angew. Chem. Int. Ed.* 47 (2008) 1766–1769.
- [48] Y. Guo, J. Li, Y. Yuan, L. Li, M. Zhang, C. Zhou, Z. Lin, *Angew. Chem. Int. Ed.* 55 (2016) 14693–14697.
- [49] J. Lee, H.S. Shim, M. Lee, J.K. Song, D. Lee, *J. Phys. Chem. Lett.* 2 (2011) 2840–2845.
- [50] Y. Li, H. Xu, S. Ouyang, D. Lu, X. Wang, D. Wang, J. Ye, *J. Mater. Chem. A* 4 (2016) 2943–2950.
- [51] M.Q. Yang, Y.J. Xu, W. Lu, K. Zeng, H. Zhu, Q.H. Xu, *Nat. Commun.* 8 (2017) 14224.
- [52] V.W.-h. Lau, V.W.-z. Yu, F. Ehrat, T. Botari, I. Moudrakovski, T. Simon, V. Duppel, E. Medina, J. Stolarczyk, J. Feldmann, V. Blum, B.V. Lotsch, *Adv. Energy Mater.* (2017) 1602251.
- [53] J. Wang, Y. Chen, Y. Shen, S. Liu, Y. Zhang, *Chem. Commun. (Camb.)* 53 (2017) 2978–2981.
- [54] K. Li, Z. Zeng, L. Yan, M. Huo, Y. Guo, S. Luo, X. Luo, *Appl. Catal. B: Environ.* 187 (2016) 269–280.
- [55] J. Ran, B. Zhu, S. Qiao, *Angew. Chem. Int. Ed.* 56 (2017) 10373–10377.
- [56] J. Ran, G. Gao, F. Li, T. Ma, A. Du, S. Qiao, *Nat. Commun.* 8 (2017) 13907.
- [57] J. Liu, Y. Liu, N. Liu, Y. Han, X. Zhang, H. Huang, Y. Lifshitz, S.-T. Lee, J. Zhong, Z. Kang, *Science* 347 (2015) 970–974.
- [58] K. Schwinghammer, B. Tuffy, M.B. Mesch, E. Wirnhier, C. Martineau, F. Taulelle, W. Schnick, J. Senker, B.V. Lotsch, *Angew. Chem. Int. Ed.* 52 (2013) 2435–2439.
- [59] Y. Ham, K. Maeda, D. Cha, K. Takanabe, K. Domen, *Chem. Asian J.* 8 (2013) 218–224.
- [60] C.J. Pedersen, *J. Am. Chem. Soc.* 89 (1967) 7017–7036.
- [61] Y. Li, S. Ouyang, H. Xu, X. Wang, Y. Bi, Y. Zhang, J. Ye, *J. Am. Chem. Soc.* 138 (2016) 13289–13297.
- [62] T. Xiong, W. Cen, Y. Zhang, F. Dong, *ACS Catal.* 6 (2016) 2462–2472.